JOURNAL OF MATERIALS SCIENCE 29 (1994) 1629–1635

Laser surface refinement of $YBa_2Cu_3O_x$ superconductor

C. H. S. SHIH, P. A. MOLIAN, R. W. McCALLUM*
*Department of Mechanical Engineering and *Ames Laboratory, Department of Materials Science and Engineering, Iowa State University, Ames, IA 50011, USA*

U. BALACHANDRAN
Energy Technology Division, Argonne National Laboratory, Argonne, IL 60439, USA

A novel laser-processing technique that produces bulk $YBa_2Cu_3O_x$ (1 2 3) plates has been developed. Through the application of a square CO_2 laser beam with uniform energy density distribution to the surface of 1 2 3 powder compact, a single piece of ribbon-like plate is produced. This plate may be separated from the powder compact after laser scanning. The width of the plate is ≈ 6 mm, while its thickness is 0.1–0.2 mm. Powder X-ray diffraction indicates that laser-treated samples contain both orthorhombic and tetragonal 1 2 3 phases, as well as Y_2O_3 (2 0 0), Y_2BaCuO_5 (2 1 1), $BaCuO_2$ (0 1 1), and CuO (0 0 1) phases. Scanning electron microscopy reveals a pattern of phase segregation along the transverse cross-section after solidification of the plate. After oxygen annealing of a single ribbon piece, T_c is found to be 90 K. This technique may be applicable to the mass production of 1 2 3 bulk superconductor by continuous melting of 1 2 3 powders. In addition to its potential for practical applications, the laser technique also helps to explain the complex phases and microstructure formation during melting and solidification of laser-melted 1 2 3 liquid. A model relating the microstructure to the thermal history inside the laser-affected region and to the phase diagram of incongruently melting 1 2 3 material has been developed to analyse phase formation during laser melting and solidification processes. Reasonable correspondence between theoretical analysis and experimental results was obtained.

1. Introduction

While the high-temperature ceramic oxide superconductors have extremely high transition temperatures, T_c, and upper critical magnetic fields, H_{c2}, their critical current, J_c, values so far are low, with the exception of those of thin films. The high T_c and H_{c2} values are characteristic properties intrinsic to the material, while the low J_c value of bulk specimens is a consequence of the fabrication process.

Typical transport J_c values at 77 K of sintered $YBa_2Cu_3O_x$ superconductors are $\approx 500\ \mathrm{A\,cm^{-2}}$ in zero field and $\approx 1\ \mathrm{A\,cm^{-2}}$ at a magnetic field of $1T$ [1, 2]. This phenomenon may be attributed to the weak link problem of grain-to-grain junctions. Jin *et al.* [3] obtained J_c as high as $17\,000\ \mathrm{A\,cm^{-2}}$ by using a melt-processing technique that induced favourable texturing and extensive grain growth but also yielded some secondary phase.

Other techniques such as melt-textured growth [4–7], quench and melt growth process [8–10], laser float zone melting [11–15], and laser surface melting [16, 17] are similar in purpose; all are aimed at eliminating or reducing the influence of weak links on critical current density. Of these techniques, the laser-related melt-processing methods are worth noting. High energy-density laser heat sources have been reported as able to heat sintered samples with 1 2 3 stoichiometry above the liquidus within a very short time in a confined region; this approach is believed to limit severe phase segregation. Under controlled cooling processes, advantageous morphologies and phase distributions have been produced.

Although all published accounts of laser-related processing of 1 2 3 material report crystallization of 1 2 3 grains and densification of microstructure from the melt–liquid state produced by laser heating, none produced laser-treated material that is separable from the laser-unaffected region. Because the unaffected region in these studies has been superconducting material, evaluation of superconducting properties of the laser-treated material is not possible. In addition, published works [16, 17] have not adequately related the phases formed during laser heating of the 1 2 3 material to the equilibrium phase diagram.

In this work, the technique of laser surface melting was applied to a stoichiometric 1 2 3 pressed powder compact with a square laser beam that had uniform energy-density distribution. A single-piece ribbon-like 1 2 3 plate with dense and fine-grained microstructure of different phases was separated from the untreated

0022–2461

base powder compact after laser melting. Thicknesses of these separated ribbon plates are in the range of 0.1–0.2 mm, while the width is ≈ 6 mm. The morphology of each phase is distributed uniformly as a function of depth and is uniform across the ribbon. Thus, unlike previous laser experiments, a one-dimensional thermal model can be used to explain the actual phase and microstructure formation of the laser-treated 1 2 3 ribbon. After oxygen annealing, the ribbon exhibits superconducting properties with a transition temperature of ≈ 90 K. This technique has the potential for continuous mass production of a uniquely laser-treated, dense, fine-grained orthorhombic 1 2 3 superconductor.

This report will describe and analyse this laser surface refinement. Powder X-ray diffraction (XRD) analysis, optical microscopy, and scanning electron microscopy (SEM), coupled with energy-dispersive X-ray spectroscopy (EDS) and chemical element analysis, were used to evaluate the influence of the laser melting on the 1 2 3 material. With these standard examination techniques, it was possible to identify phases produced after solidification, as well as the morphology of these phases within a transverse cross-sectional area of the 1 2 3 separated plate. Thermal phenomena relating to the interactions between laser light and the 1 2 3 ceramics powder compact, including heat-transfer models, temperature profiles, and melting and solidification behaviour of the laser-melted layers, are discussed. A comparison between the theoretical model and the microstructure of the separated 1 2 3 ribbon results in general agreement between the two. The lack of detailed agreement arises from the simplifying assumptions made in the model.

2. Experimental procedure

The 1 2 3 powders were prepared by vacuum calcination from CuO, Y_2O_3, and $BaCO_3$ precursors [18]. Approximately 20 g powder were loaded into a die having a 4.45 cm diameter. The powder was cold-pressed uniaxially at 55 MPa and then the resulting pellet used as the starting material for the laser surface refinement experiments.

A continuous-wave 1000 W CO_2 gas transport laser was used to study the laser-melting effect on 1 2 3 powder compacts. The output beam had a diameter of 19 mm and a Gaussian energy distribution (TEM_{00}). An optical integrator formed the circular laser beam into a square spot measuring 6.35 mm on each side. The powder compact was placed on an $X-Y$ table whose motion was controlled by a computer numerical controller. A single laser pass was made on the powder compact by moving the specimen at speeds of 21.2–84.7 mm s^{-1}. After laser scanning, the melted surface layer solidified and separated from the 1 2 3 powder compact base pellet, with some loose 1 2 3 powders adhering to the bottom of the plate. This laser-treated ribbon was collected and the adhering powders cleaned away with an ultrasonic cleaner.

As-treated ribbons were analysed as described below. To obtain the maximum orthorhombic 1 2 3 phase composition, laser-treated ribbons were oxygen-annealed. The samples were placed in an MgO crucible in a furnace under 1 bar of flowing oxygen, and the temperature was ramped at a rate of 5 °C min^{-1} to 900 °C. Following a hold at 900 °C for 24 h, the sample was then cooled to 450 °C over 24 h. A 24 h hold at 450 °C, followed by cooling to room temperature at 5 °C min^{-1}, was used to oxygenate the sample.

For metallographic examination, the laser-scanned ribbon was mounted to expose the transverse cross-section area. Standard polishing procedures were used. Both laser-treated specimens (as-treated and as-annealed) were examined for microstructure with a high-resolution optical microscope. Powder X-ray diffraction (XRD) with a GE diffractometer and CuK_α radiation, together with SEM, were used to characterize the samples. XRD specimens were ground to avoid any preferred orientation that might be present in the laser-treated ribbons and to avoid surface segregation effects. To identify the phases present, the peaks were matched with standard patterns. For SEM examination, both secondary electron image mode and backscattered electron image mode were used to obtain the necessary information from cross-sectional samples. EDS was used to identify the phases. A small piece of laser-treated 1 2 3 separated plate was ground into fine powder for chemical element analysis. Magnetization measurements were made in a Quantum Design magnetometer; both zero-field and field-cooled procedures were used to determine superconducting properties.

3. Results

The low-magnification micrographs in Fig. 1 are cross-sectional cuts that show the uniform thickness (0.1–0.2 mm) of the square-beam laser-treated sample. As indicated, the laser was incident on the upper edge. The scanning direction was perpendicular to the plane of the micrograph. Minor longitudinal cracks are shown by the secondary-image scanning electron micrograph on the left. In the enlarged optical micrograph on the right, a dense, continuous structure can be seen in the centre and surface region, while porosity and second-phase segregation appear in the bottom layer. The high-resolution scanning electron micrograph on the left of Fig. 2 shows another characterization of a laser-treated sample. At the edge of the surface layer, extremely fine-grained structure is observed. The orientation of the micrograph is as in Fig. 1.

Fig. 3 shows the powder XRD results of both laser-treated and oxygen-annealed samples. In the pattern for the laser-treated sample, the split peak near the 33° 2θ value was characterized as the coexistence of both tetragonal and orthorhombic structure of $YBa_2Cu_3O_x$ stoichiometry, based on the equal intensity of the two peaks. Major 2 1 1 peaks also appear near 29° and 30° 2θ. The existence of $BaCuO_2$ in the laser-treated compound is characterized by the peaks marked by triangles. In addition, Y_2O_3 and Cu_2O are also detected, as indicated in Fig. 3. After oxygen-annealing, the tetragonal 1 2 3 is completely

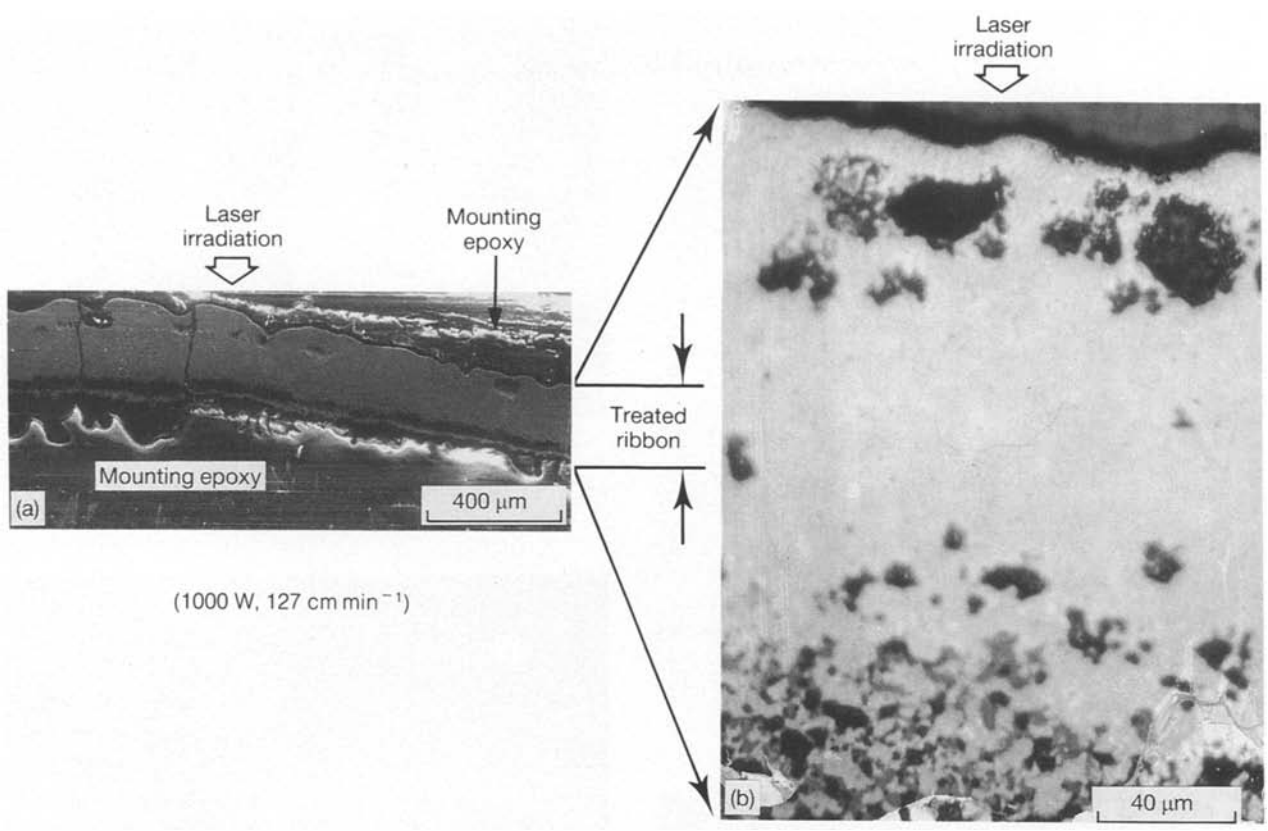

Figure 1 Typical cross-sections of a laser-treated sample: (a) SEM cross-section, (b) optical cross-section.

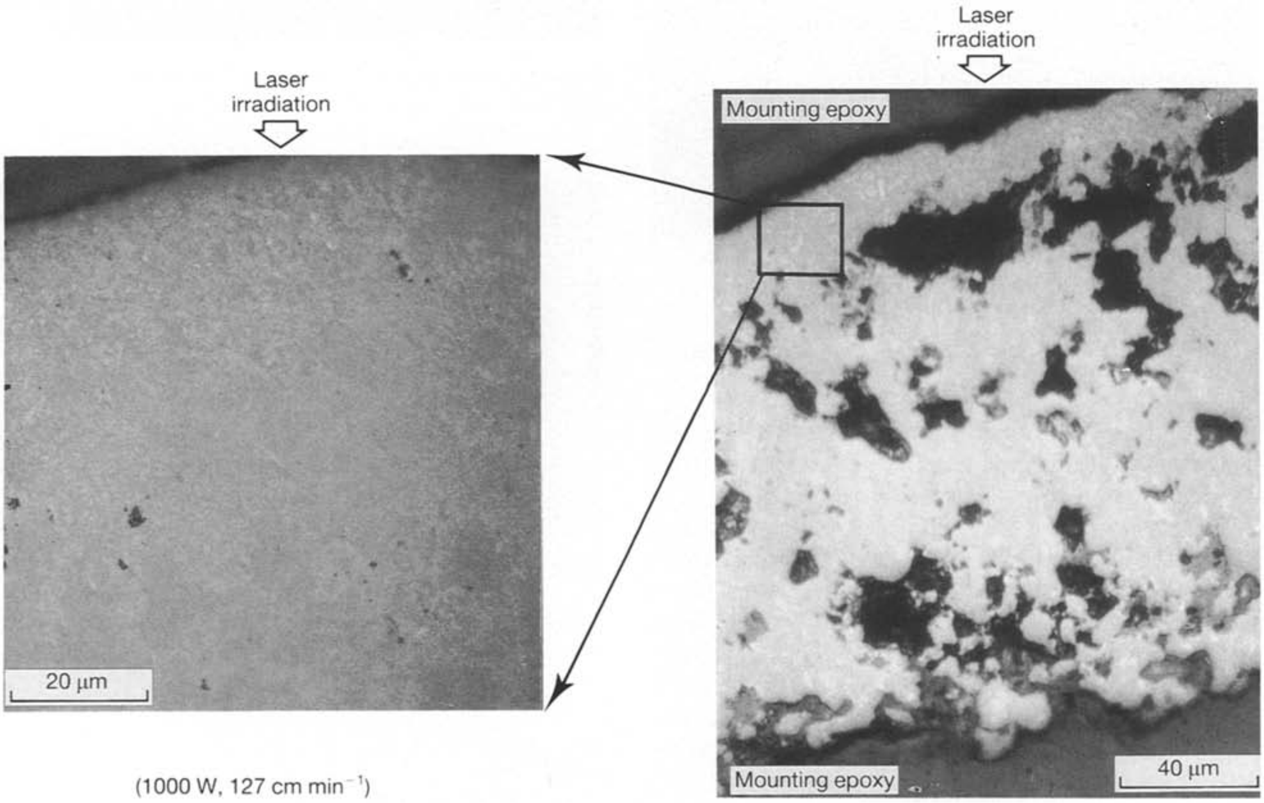

Figure 2 Fine-grained images at the surface edge of a laser-treated sample.

transformed into orthorhombic 1 2 3 (cross mark), while the 2 1 1, $BaCuO_2$, and Y_2O_3 exist even after oxygen-annealing.

Details of the microstructure are revealed in back-scattered SEM images of a polished transverse cross-section of a laser-treated 1 2 3 ribbon. Fig. 4 is the magnified surface region of a laser-treated ribbon-like plate. Tiny particles with darker colours are isolated in a mass-matrix material of lighter colour. These particles are approximately spherical and their sizes

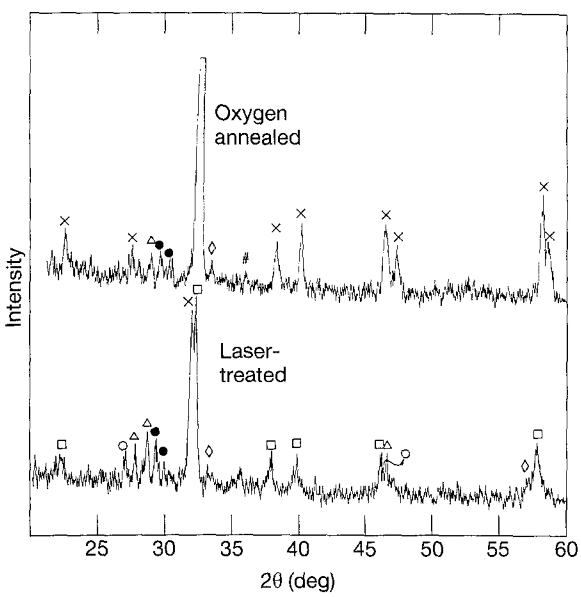

Figure 3 Powder X-ray diffraction analysis on as-laser-treated and as-oxygen-annealed samples. (×) 1 2 3 (orthogonal), (□) 1 2 3 (tetragonal), (△) $BaCuO_2$, (○) $BaCO_3$, (●) 2 1 1, (◇) Y_2O_3, (#) Cu_2O.

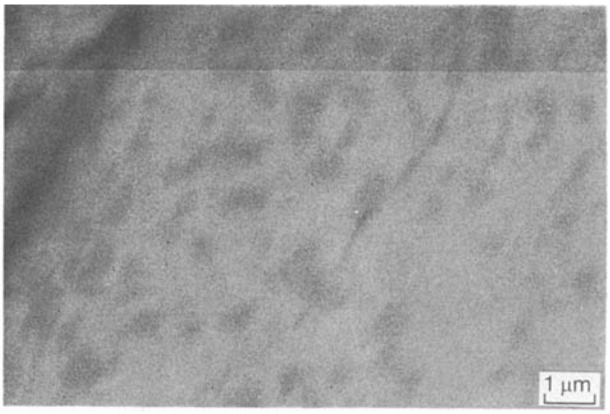

Figure 4 Magnified surface region of a laser-treated plate.

are 0.5–1 μm. With EDS analysis mode, these tiny particles can be identified as 2 0 0 (Y_2O_3) phase, while the matrix material is identified as 1 2 3 phase.

Fig. 5 shows a mixed state of faceted grains surrounded by some darker phase in the deeper region directly below the surface area. This darker phase tends to be continuous. With EDS analysis, the faceted grains are identified as 2 1 1 (Y_2BaCuO_5), while the surrounding phase is 0 1 1 ($BaCuO_2$). In addition to the 2 1 1 and 0 1 1 phases, 1 2 3 phase is also detected, as labelled in Fig. 5. Fig. 6 shows the microstructure in the central region of a laser-treated 1 2 3 plate. An irregularly mixed state of two phases can be seen in this figure. The darker phase is identified through EDS analysis as 1 2 3 phase. The lighter-coloured phase is found to be 0 1 1 ($BaCuO_2$). Fig. 7 shows the magnified microstructure of the bottom layer, but does not indicate clear discrimination between different phases. However, some regions feature the grain-boundary structure, with minor dark spots identified as 0 0 1 (CuO) phase. Near this grain-boundary region, 1 2 3 and 0 1 1 phases are identified by EDS.

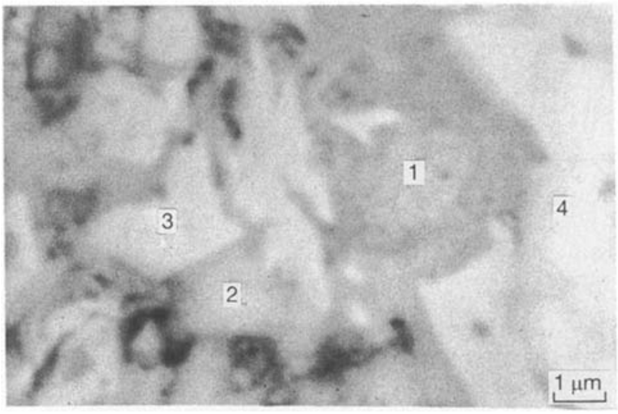

Figure 5 Surface region at deeper depth than in Fig. 4; spots 1 and 2 are 0 1 1 phase, spot 3 is 2 1 1 phase, and spot 4 is 1 2 3 phase.

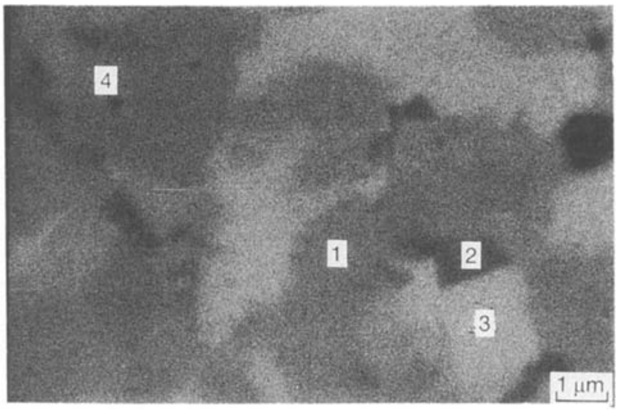

Figure 6 Central region of a laser-treated plate; spots 1 and 4 are 1 2 3 phase, and spots 2 and 3 are 0 1 1 phase.

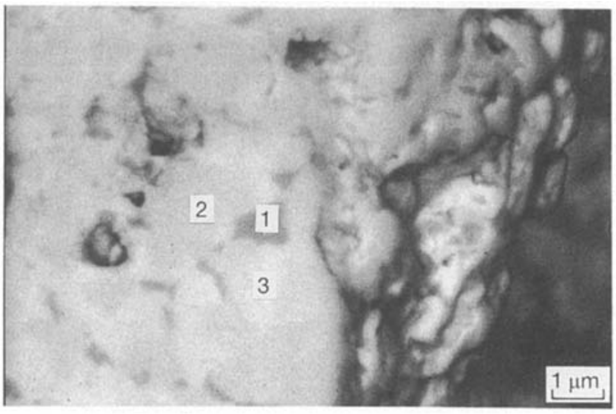

Figure 7 Bottom region of a laser-treated plate; spot 1 is CuO (0 0 1) phase, spot 2 is 1 2 3 phase, and spot 3 is $BaCuO_2$ (0 1 1) phase.

The average chemical composition of the laser-treated material was determined by wet chemical analysis. The weight per cent ratio between yttrium, barium and copper was found to be 13.1:38.7:27.5 for the laser-treated sample, and 13.1:39.1:27.9 for the oxygen-annealed sample. This corresponds to the 1 2 3 starting stoichiometry and indicates that no preferential loss of elements from the laser-melted layer occurred through surface evaporation or interface diffusion.

Thus, mass conservation can be ensured for these three elements during laser melting, resolidifying, and separating processes.

Fig. 8 is the magnetization versus temperature curve of an as-oxygen-annealed sample for both zero-field cooled (ZFC) and field cooled (FC) measurements. The FC measurement exhibits a relatively sharp transition at 90 K, and shape of the curve shows the effect of the fine grain size obtained in this process. The ZFC transition is characteristic of weak linking of these grains.

4. Discussion

During the laser surface heating process, the thermal history inside the laser-affected region is complicated and determines the phase formation of the final separated 1 2 3 ribbon. The interrelationship among thermal history, phase diagram, and final microstructure will be demonstrated by discussing two simplified models, one for pure metals and the other for the 1 2 3 superconductor. In both models, four important assumptions are made: (a) only surface melting occurs in the laser-treated region, and no surface evaporation takes place; (b) all temperature variations and phase formations are considered to be in one direction. This assumption is valid if the width of the melted zone is large compared to the melt depth; (c) the material is homogeneous with constant properties, i.e. the effects of macroscopic diffusion and phase separation are negligible; (d) no latent heat was consumed during melting or released during solidification.

Under these four assumptions, it is possible to calculate temperature profiles during laser heating and melting of the material surface at some presumed position along the laser-beam scanning path. These profiles are derived from an analytical solution of energy equations as follows:

$$T(x, t) = q_0/k\{(4at/\pi)^{1/2}\mathrm{e}^{-[x/(4at)^{1/2}]^2} - x\,\mathrm{erfc}[x/(4at)^{1/2}]\} + T_0 \qquad (1)$$

where q_0 is the absorbed power density, a the thermal diffusivity, k the thermal conductivity, erfc a complimentary error function, and T_0 the room temperature.

Because melting of pure metals occurs at a unique temperature, only two-phase fields exist as a function of depth under the laser beam. At an arbitrary position in the path of the laser scan, the melt will propagate from surface to a depth, d, during a time span, $t_{\max} = d_1/v$, where d_1 is the dimension of the square laser beam and v is the scan velocity. Typical experimental values of $d_1 \approx 6$ mm, and $v \approx 21$ mm s^{-1} give a $t_{\max}$ of 0.3 s.

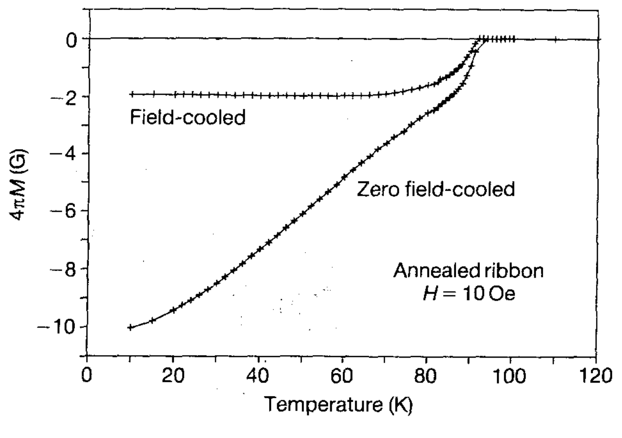

Figure 8 T_c measurement curve.

For a noncongruently melting material such as the peritectic 1 2 3, the melt divides into a number of layers in the absence of stirring. Referring to the isopleth along the 2 1 1 and 0 1 1 tie line of the 1 2 3 ternary phase diagram and using heating profiles as in Fig. 9, one obtains two regions of partial melting below the liquid surface layer. The liquid layer is on the surface, labelled d1. The region labelled d2 consists of 2 0 0 plus liquid phase. The region d3 is occupied by 2 1 1 plus liquid phase. Because the time above the appropriate decomposition temperature will vary as a function of depth, the grain size of the solid component (2 1 1 or 2 0 0) in the solid/liquid two-phase region will also vary as a function of depth in the region.

So far, we have only considered what happens during heating of the surface. The differences between our two models extend to the cooling of the laser-melted surface as well. In the cooling of surface-melted pure metal, the bulk of the material unaffected by the laser below the melted surface layer acts as a massive heat sink that conducts away and absorbs the heat from the surface layer. The radiation and convection heat transfer to the atmosphere from the melted surface layer can be neglected for this special case, due to the high metallic thermal conductivity and good thermal contact with the solid substrate. Much more heat is dissipated from the surface by conduction into the bulk than by radiation and convection from the surface.

For a ceramic powder compact, however, heat transfer is very different. The heat-transfer mechanism of metal is largely through conduction electrons, with an additional phonon contribution. For insulating ceramics, such as tetragonal 1 2 3, however, the conduction electron contribution is greatly reduced, resulting in a thermal conductivity in ceramic materials that is orders of magnitude lower than that in metals. When these ceramic powders are pressed

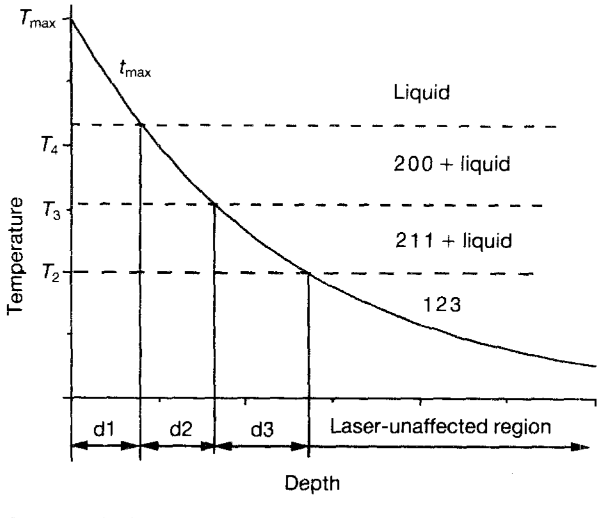

Figure 9 Final temperature profile and phase formation at various transition temperatures as a function of depth.

together under pressure, the heat-transfer model becomes a composite case of ceramic solid particles and air gaps. The heat fluxes that can be conducted away from the laser-melted surface layer downward through different media, e.g. metal and ceramic powder compact, are greatly different. Calculated under the same temperature difference and conducting thickness, the ratio between thermal conductivities for a metallic conductor and a powdered ceramic compact can reach $10^4:1$. According to the Stefan–Boltzmann law $E = \varepsilon s T^4$, where ε is the emissivity of ceramics, and s is the Stefan–Boltzmann constant. Emissivity for most of the ceramics and minerals is in the range of 0.8–1, while that of metals is 0.02–0.2 [19]. Thus, we conclude that the surface of a metal will cool by thermal conduction to the bulk of the material, while the surface of the ceramic powder compact will cool primarily by radiation.

The average cooling rate of the laser-affected region of 1 2 3 ceramics may be estimated by assuming a constant temperature distribution inside the cooling liquid region, radiation only from the surface, and no heat conduction through the base powder compact. By using approximate values of thermal properties of 1 2 3 material, i.e. heat capacity $= 0.2\,\mathrm{cal\,g^{-1}K^{-1}}$, density $= 6.4\,\mathrm{g\,cm^{-3}}$, we obtain an average cooling rate of $\approx 10^3\,^\circ\mathrm{C\,s^{-1}}$ on the 1 2 3 surface layer. According to this analysis, the laser-melted layer of pure metal will undergo an extremely high cooling rate, and a layer of amorphous structure will very possibly form after solidification. For the ceramic material, the cooling rates are much lower, and are highest at the surface.

To understand the final microstructure obtained from the above process, we must consider the solidification path for each layer. The simplest layer to consider is that of 2 1 1 plus liquid. When 1 2 3 is heated to temperature T_2 in Fig. 10, it decomposes into 2 1 1 and a liquid at composition C_2. If this mixture is suddenly cooled below the decomposition temperature of 1 2 3 to temperature T_1 and held, a small amount of 1 2 3 will precipitate out of the liquid so that the liquid composition becomes C_1. In order for more 1 2 3 to be formed, the 2 1 1 that formed at the higher temperature must dissolve into the liquid [20] as the 1 2 3 precipitates, to maintain the proper composition of the melt. Because diffusivity in the melt is very high, the rate-limiting step is clearly the dissolution rate of the 2 1 1. If the temperature is lowered below the ternary eutectic temperature, solid-state diffusion is required and then becomes the rate-limiting step. If the cooling time from T_2 to below T_1 (1 2 3 + $BaCuO_2$ + CuO + liquid) is short compared to the time required to dissolve significant amounts of 2 1 1, the solidified structure will consist primarily of 2 1 1 and the Ba–Cu–O phases.

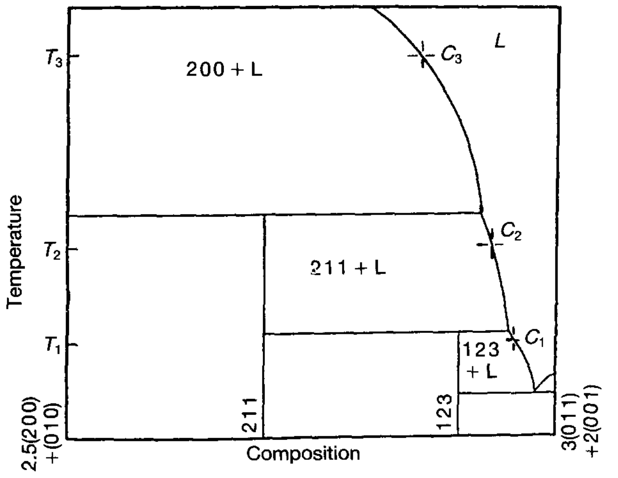

Figure 10 Pseudobinary phase diagram of Y–Ba–Cu–O system.

If the maximum temperature reached is T_3, the decomposition products are 2 0 0 and a liquid whose composition lies outside the plane of our isopleth but that is approximated by C_3. When the mixture is cooled to T_2, 2 1 1 is immediately precipitated to bring the liquid composition to C_2; in analogy to the above discussion, however, further precipitation of 2 1 1 requires the dissolution of 2 0 0.

From this discussion, it is clear that when the maximum temperature does not exceed the liquidus, and when the quench rate exceeds the rate at which the solid can be dissolved into the liquid, the phase composition of the as-quenched material is determined by the maximum temperature reached. The rate at which the solid is dissolved will be determined by the kinetics at the interface (which for a compound can be quite slow) and by the surface area of the interface, i.e. the particle size of the solid.

When the liquidus is exceeded, the maximum temperature state is finally uniform. Unlike the two previous cases, it is now possible to undercool to the point at which large amounts of 1 2 3 are formed directly from the melt. Lesser degrees of undercooling will result in 2 1 1 or 2 0 0 formation. The initial quench rate of the melt now becomes a highly significant factor in the final microstructure.

Experimentally, we can obtain an idea of the rate at which 2 0 0 and 2 1 1 dissolve into the liquid, based on results of drop-tube experiments [21]. For 150–200 µm spheres dropped in oxygen through 1500 °C, particles of 2 0 0 of the order of 10 µm are embedded in a solidified liquid matrix. X-ray diffraction of the crushed spheres shows minimal formation of 1 2 3. Because the cooling rate of the spheres is expected to be $\approx 10^2$–$10^3\,^\circ\mathrm{C\,s^{-1}}$, it is clear that 2 0 0 dissolves very slowly. Similar data are not available for spheres heated into the 2 1 1 stability region because lower furnace temperatures resulted in non-spherical particles; this suggests non-uniform decomposition of the particles. However, bulk samples of several grams removed from a conventional furnace consist primarily of 2 1 1 and not 1 2 3, thus confirming that 2 1 1 also dissolves very slowly in the liquid. This means that any quench rate above the 10^2–$10^3\,^\circ\mathrm{C\,s^{-1}}$ range is essentially infinite for samples cooled from below the liquidus as far as the 2 1 1 or 2 0 0 constituent is concerned.

Having established that for the quench rates achieved in laser surface treating, 2 0 0 or 2 1 1 will be retained during quenching from the respective areas of the phase diagram, we can now evaluate microstructures resulting from non-uniform heating of the sample. SEM examination of the ribbon shows a surface layer of 1 2 3 with a relatively uniform dispersion of fine 2 0 0 particles. This layer is the result of the relatively rapid quenching of the fully molten surface layer. The quench rate was not rapid enough to suppress completely the formation of 2 0 0 but sufficiently rapid to pass through the 2 1 1 phase field with little formation of 2 1 1. Below this layer, 2–3 μm grains of 2 1 1 are surrounded by 0 1 1; there is also some 1 2 3 in this region. We associate this layer with material that was heated into the 2 1 1 stability range. The layer heated to the 2 0 0 stability range is missing; because it has a large fraction of liquid, this layer was probably mixed with the molten surface layer by convection currents. The base layer of the ribbon is 1 2 3 surrounded by 0 1 1. The previously advanced model does not account for this layer, but the phase diagram shows that this layer did not exceed the decomposition temperature of 1 2 3. Because the ternary eutectic is significantly lower than the decomposition temperature, liquid from the warmer layers is free to flow into this region and cement the 1 2 3 grains together.

5. Conclusions

From this experiment, the effects of integrator laser-beam irradiation on 1 2 3 powder compact are concluded as follows.

1. A single piece of laser-treated ribbon-like plate with a dense, fine-grained superconducting microstructure can be obtained through melting, resolidification, and separation from a base unsintered 1 2 3 powder matrix. T_c is ≈ 90 K.

2. This technique has an important advantage over other laser-treatment approaches. That is, it explains the phases and microstructure formation during laser melting and solidification of the 1 2 3 superconductor, which has a complicated phase diagram in the high-temperature range. Because this technique can produce a uniformly melted laser-affected region with uniformly distributed phases and morphology across its width, a reasonably simplified thermal model can be developed to explain the melting and solidification processes.

3. The experimentally determined microstructure of laser-treated 1 2 3 ribbon using SEM analysis, XRD, and chemical element analysis are consistent with the microstructure and phase formation derived from the proposed thermal model.

4. The existence of an as-treated orthorhombic 1 2 3 phase in the powder XRD examination of a laser-treated sample can be explained in terms of a very thin surface layer of the laser-separated plate. This layer has been hypothesized to form as a result of a large undercooling of the melt from above the liquidus temperature ($>1500\,^{\circ}$C). The layer is thin enough that significant oxygenation occurs during the subsequent cooling to room temperature, resulting in a partial transformation of the tetragonal 1 2 3 to orthorhombic 1 2 3.

5. Because the laser-treated material may be separated from the untreated base material, extensive analysis is now possible. This includes powder X-ray diffraction analysis and determination of superconducting properties.

6. Laser treating by this method produces a relatively uniform dispersion of fine-grained second phases, e.g. 2 1 1 and Y_2O_3, in the 1 2 3 matrix; if properly controlled, this method may result in enhanced critical current due to flux pinning.

Acknowledgements

This work was supported by the US Department of Energy, Efficiency and Renewable Energy, as part of a programme to develop electric power technology, under Contract W-31-109-Eng-38; and Office of Basic Energy Sciences, under Contract W-7405-Eng-82. Technical assistance from T. J. Folkerts, M. J. Kramer, K. W. Dennis, R. H. Lee and S. Wu is greatly appreciated.

References

1. B. YARAR, J. TREFNY, F. SCHOWENGERDT, N. MITRA and G. PINE, *Adv. Ceram. Mater.* **2** (1987) 372.
2. D. C. LARBALESTIER, D. MAEUMLING, X. CAI and J. SEUNTJENS, *J. Appl. Phys.* **62** (1987) 3308.
3. S. JIN, R. C. SHERWOOD, T. H. TIEFEL, R. B. VANDOVER, D. W. JOHNSON and G. S. GRADER, *Appl. Phys. Lett.* **51** (1987) 855.
4. S. JIN, T. TIEFEL, R. SHERWOOD, R. VANDOVER, M. DAVIS, G. KAMMLOTT and R. FASTNACHT, *Phys. Rev. B* **37** (1988) 7850.
5. S. JIN, T. H. TIEFEL, R. C. SHERWOOD, M. E. DAVIS, R. D. VANDOVER, G. W. KAMMLOTT and H. D. KEITH, *Appl. Phys. Lett.* **52** (1988) 2074.
6. S. JIN, R. SHERWOOD, E. GYORGY, E. TIEFEL, R. VANDOVER, S. NAKAHARA, R. FASTNACHT and M. DAVIS, *ibid.* **54** (1989) 584.
7. J. D. ALFORD, W. J. BIRCHALL, W. J. CLEGG and K. KENDALL, *J. Appl. Phys.* **65** (1989) 2856.
8. Y. YANG, S. ASHWORTH, C. BEDUZ, R. G. SCURLOCK, R. WEBB and Z. YI, *Supercond. Sci. Technol.* **3** (1990) 282.
9. M. MURAKAMI, M. MORITA and N. KOYAMA, *Jpn J. Appl. Phys.* **28** (1989) 1125.
10. S. X. DOU, H. K. LIU, M. H. APPERLEY, K. H. SONG and C. C. SORRELL, *Supercond. Sci. Technol.* **3** (1990) 138.
11. S. W. HSU, K. CHEN and W. H. LEE, *Solid State Commun.* **75** (1990) 799.
12. D. GAZIT and R. S. FEIGELSON, *J. Cryst. Growth* **91** (1988) 318.
13. M. LEVINSON, S. P. SHAH and D. Y. WANG, *Appl. Phys. Lett.* **55** (1989) 1683.
14. X. JIANG, X. HUANG, Y. YU, M. JIANG, G. QIAO, G. GE, Z. HU, C. SHI, Y. ZHAO, Y. WANG, G. XU and Y. ZHOU, *Supercond. Sci. Technol.* **1** (1988) 102.
15. Z. XU, P. D. HAN, L. CHANG, A. SHANA and D. A. PAYNE, *J. Mater. Res.* **15** (1990) 39.
16. G. HOFER, W. KLEINLEIN and B. C. FRIEDRICH, *Acta Metall.* **44** (1990) 1142.
17. U. VARSHNEY, R. L. CHURCHILL, J. M. GLASS and A. I. KINGON, *Supercond. Sci. Technol.* **3** (1990) 385.
18. U. BALACHANDRAN, R. B. POEPPEL, J. E. EMERSON, S. A. JOHNSON, M. T. LANAGAN, C. A. YOUNGDAHL, D. SHI, K. C. GORETTA and N. G. EROR, *Mater. Lett.* **8** (1989) 454.
19. J. H. LIENHARD (ed.), "A Heat Transfer Textbook", 2nd Edn (Prentice Hall, Boston, 1987) pp. 67–9.
20. B. J. CHEN, M. A. RODRIGUEZ, S. T. MISTURE and R. L. SNYDER, *Phys. C* **198** (1992) 118.
21. T. J. FOLKERTS, M. J. KRAMER, K. W. DENNIS and R. W. McCALLUM, *J. Mater. Res.* **6** (1991) 2035.

Received 5 May
and accepted 25 August 1993